Environmental Science & Technology

pubs.acs.org/est

Article

Efficient CO_2 Conversion through a Novel Dual-Fiber Reactor System

Published as part of Environmental Science & Technology virtual special issue "Accelerating Environmental Research to Achieve Sustainable Development Goals".

Tzu-Heng Wang, YenJung Sean Lai,* Cheng-Kuo Tsai, Han Fu, Ruey-An Doong, Paul Westerhoff,* and Bruce E. Rittmann

Cite This: *Environ. Sci. Technol.* 2024, 58, 13717−13725

Read Online

ACCESS | Metrics & More | Article Recommendations | Supporting Information

ABSTRACT: Carbon dioxide (CO_2) can be converted to valuable organic chemicals using light irradiation and photocatalysis. Today, light-energy loss, poor conversion efficiency, and low quantum efficiency (QE) hamper the application of photocatalytic CO_2 reduction. To overcome these drawbacks, we developed an efficient photocatalytic reactor platform for producing formic acid (HCOOH) by coating an iron-based metal−organic framework (Fe-MOF) onto side-emitting polymeric optical fibers (POFs) and using hollow-fiber membranes (HFMs) to deliver bubble-free CO_2. The photocatalyst, Fe-MOF with amine-group ($-NH_2$) decoration, provided exceptional dissolved inorganic carbon (DIC) absorption. The dual-fiber system gave a CO_2-to-HCOOH conversion rate of 116 ± 1.2 mM h^{-1} g^{-1}, which is ≥18-fold higher than the rates in photocatalytic slurry systems. The 12% QE obtained using the POF was 18-fold greater than the QE obtained by a photocatalytic slurry. The conversion efficiency and product selectivity of CO_2-to-HCOOH were up to 22 and 99%, respectively. Due to the dual efficiencies of bubble-free CO_2 delivery and the high QE achieved using the POF platform, the dual-fiber system had energy consumption of only 0.60 ± 0.05 kWh mol^{-1}, 3000-fold better than photocatalysis using slurry-based systems. This innovative dual-fiber design enables efficient CO_2 valorization without the use of platinum group metals or rare earth elements.

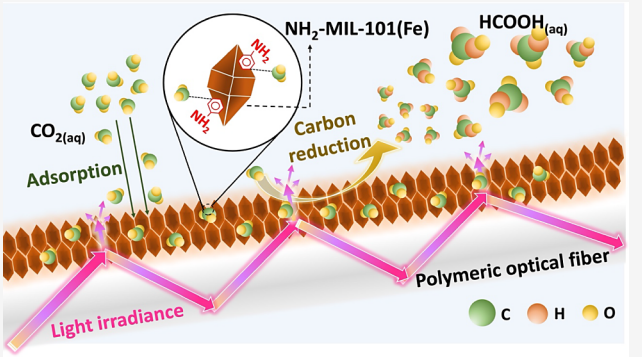

KEYWORDS: *CO_2 reduction, photocatalysis, NH_2 metal−organic framework, polymeric optical fiber, hollow-fiber membranes*

1. INTRODUCTION

Greenhouse gases (GHGs) trap heat and lead to global warming and severe effects of climate change.[1] GHG increases are mainly attributed to human activities, and the total GHG emissions by the economic sector in 2021 were 6340 million metric tons of CO_2 equivalents.[2] Carbon dioxide (CO_2) is the major GHG, and its capture before entering the atmosphere is an important mitigation approach. Captured CO_2 from point emission sources or via direct air capture (DAC) can be geologically sequestered or converted biologically or via photo- or electrocatalytic technologies into valuable chemical feedstock that can replace fossil feedstock.[3]

Photocatalytic valorization of CO_2 into organic chemicals, mimicking natural photosynthesis, is a promising approach for capturing and beneficially reusing CO_2.[4] The reduction of CO_2 into one-carbon formic acid (HCOOH) or methanol (CH_3OH), two-carbon ethanol (C_2H_5OH), or longer-chain organic products holds promise to replace petrochemical sources or traditional agricultural processes.[5] Today, HCOOH has emerged as a crucial precursor for value-added organic products,[6] but the efficiency of CO_2 reduction to formic acid is relatively poor[7] (typically higher than 10^3 kWh mol^{-1} in photocatalytic-slurry reactions).[8] Developing a more efficient and sustainable platform for CO_2 reduction to formic acid is an essential step for CO_2 valorization.

While photocatalysis (PC) has the capability to harness the entire solar spectrum, including ultraviolet, visible, and infrared wavelengths, photocatalysts that respond to visible light are preferred because visible light constitutes 45−50% of the solar spectrum and the efficiency of irradiation from light-emitting diodes (LEDs) is progressively increasing in the visible-light spectrum,[9] which enables LED technology to be used in nonsolar-based engineered reactor systems. Despite the recent advances in photocatalysts, the reactor configuration for the photocatalytic application (i.e., light-absorption plus conversion of reactants to products) is still in an early

Received: December 6, 2023
Revised: July 16, 2024
Accepted: July 17, 2024
Published: July 27, 2024

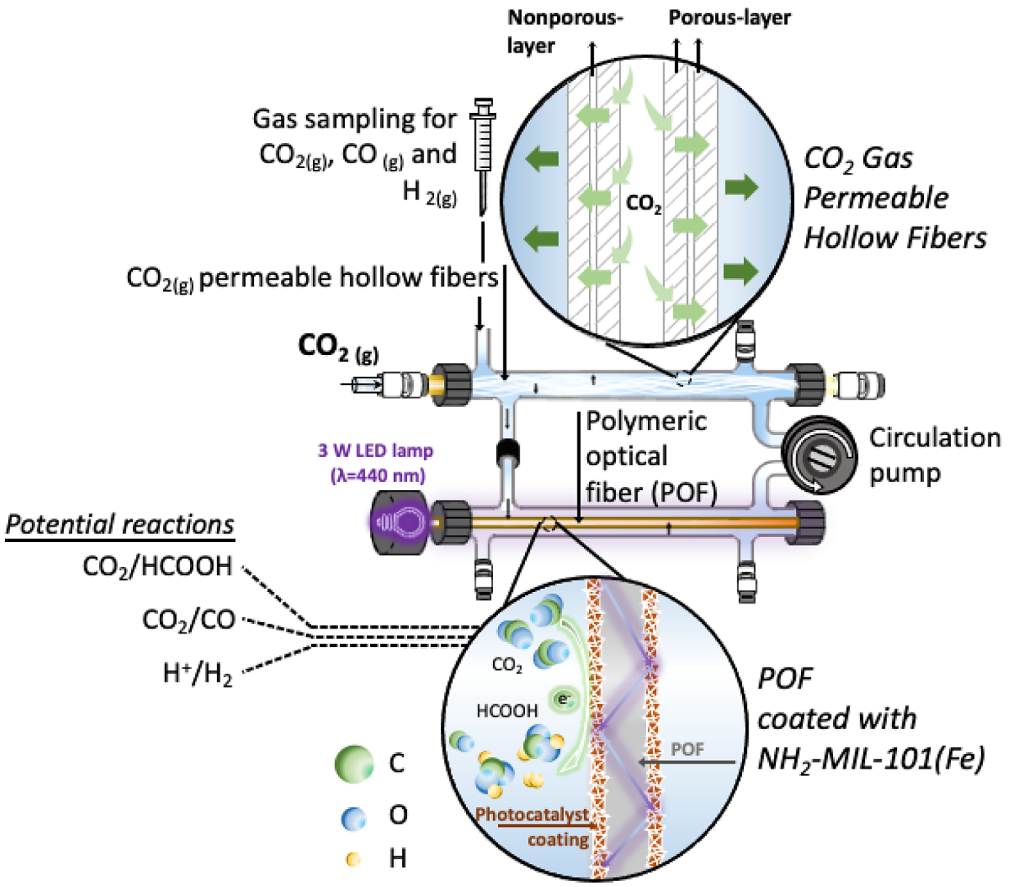

Figure 1. Schematic illustration of photocatalytic HCOOH production in the dual-fiber reactor system, including polymeric optical fibers coated with the NH_2-MIL-101(Fe) photocatalyst and hollow-fiber membranes for CO_2 delivery.

phase.[11,12] Current reactor configurations (i.e., slurry, photocatalytic film in glass, and membrane architectures) also limit the effects of light-driven catalysis. Improvements in the overall light-based conversion of CO_2 to beneficial organic carbon products can be made in three categories: (1) material properties of photocatalysts, (2) light delivery to the surface of photocatalysts, and (3) CO_2 interactions with active sites of the catalyst.[7]

Metal−organic frameworks (MOFs), a class of compounds consisting of metal ions or clusters coordinated with organic ligands to form one-, two-, or three-dimensional structures, are visible-light responsive and increasingly being used in electrocatalysis and photoreaction.[10] As CO_2-reduction catalysts, MOFs have numerous advantages over common photocatalysts, such as TiO_2 and C_3N_4, in terms of physiochemical properties: higher porosity, better thermal stability, a more durable nanostructure, and better adsorption capacity for CO_2.[13,14,16] Among the MOFs, Fe-based MOFs have proven to be highly effective for photocatalytic CO_2 reduction, outperforming other isostructural MOF candidates (e.g., Cu-MOF and Ni-MOF) and producing valuable organic products with superior conversion efficiency.[15,16] Photocatalytic CO_2 reduction should be improved even more by having a photocatalyst surface with a higher CO_2 affinity. Decorating the Fe-based MOF with the functional group $-NH_2$ creates a resonance effect with the carbonyl group (C═O), which increases CO_2 adsorption.[17] Thus, we hypothesize that an NH_2−Fe-based MOF will enhance the CO_2-reduction kinetics.

For simultaneous light delivery and CO_2 interactions, most catalysts have been evaluated in either slurry or coated flat-plate systems with a high-power light source that irradiates the entire liquid reactor in which $CO_{2(g)}$ was delivered via bubbling. We hypothesize that >10-fold improvements in light conversion efficiency of CO_2 to a valorized product can be achieved with a new photocatalytic reactor, the dual-fiber reactor, illustrated in Figure 1. The dual-fiber reactor combines a polymeric optical fiber (POF) onto which the MOF-based catalyst is coated and hollow-fiber membranes (HFM)[18] to deliver CO_2 gas without bubble formation. Bubble-free delivery of dissolved $CO_{2(aq)}$ through HFMs enables close to 100%-efficient $CO_{2(g)}$ transfer by eliminating CO_2 off-gassing associated with bubble sparging.[19] Compared to current systems for catalysis with CO_2 delivery, the dual-fiber platform should greatly improve light-harvesting efficiency; interactions among molecular $CO_{2(aq)}$, photogenerated electrons (e^-), and protons (H^+); and the catalyst reuse.[15,20]

The aims of this study were to (1) integrate the nanostructured NH_2-MIL-101(Fe) onto the POF to improve the light-harvesting and CO_2 adsorption ability; (2) quantify photocatalytic CO_2-to-HCOOH evolution and production stability within the process; and (3) evaluate the quantum efficiency and selectivity for carbon-based products. We also discuss the research's potential for scale-up and its environmental implications.

https://doi.org/10.1021/acs.est.3c10274
Environ. Sci. Technol. 2024, 58, 13717−13725

2. MATERIALS AND METHODS

2.1. Fabrication of POF-NH_2-MIL-101(Fe). Poly(methyl methacrylate)-polymeric optical fibers (POF, CK-120, 3.0 mm diameter, refractive index of 1.49) were obtained from Industrial Fiber Optics (AZ, USA). The parameters and pretreatment process (i.e., polishing of the cut surface) were the same as in the previous research.[14] Figure S1 shows that the cut surfaces on both sides of bare and modified POFs had uniform surfaces that reproducibly transmitted light into the lumen of the fiber.

NH_2-MIL-101(Fe) was attached to a POF by a dip-coating method using a prepared slurry of the MOF. NH_2-MIL-101(Fe) was prepared by following previously reported procedures with some modifications, and the characterization methods (i.e., XRD, FTIR, XPS, UV−visible, UPS, and SEM) are described in Figures S2−S7.[21,22] A well-dispersed slurry with concentrations from 1 to 10 g L^{-1} was produced by adding fixed NH_2-MIL-101(Fe) masses into 30 mL of isopropanol containing 15% of a 5% Nafion polymer solution; this mixture was stirred and sonicated for 2 h in an ice bath. As-received POFs were dip-coated into the NH_2-MIL-101(Fe) solution for 2 seconds, followed by oven-drying for 2 min at 60 °C, rinsing with DI water, and drying for 12 h at 60 °C. The modified POFs were decorated with NH_2-MIL-101(Fe) using dip-coating twice into NH_2-MIL-101(Fe) slurries, with concentrations ranging between 0 and 10 g L^{-1}. MOFs were well affixed to the POF surface in a semiporous coating, similar to other nanoparticle-coated POFs.[18] Mass loadings (μg cm^{-2}) of iron (Fe) ranging from 10 to 56 μg cm^{-2} (Table S1) were quantified by ICP-MS.

2.2. Membrane Carbonation Using Hollow-Fiber Membranes. To deliver bubble-free CO_2 into the reactor, 8 composite hollow-fiber membranes (200 μm inner and 280 μm outer diameter with 15 cm length; Model MHF 200TL, Mitsubishi Rayon, Japan) were bundled together at both ends using polyurethane tubing (1/4 inch diameter, Surethane NSF-51, ATP, USA) (details are in Supporting Information). Prior to use, fiber bundles underwent a leak test at 10 psig (corresponding to 24.7 psia or 1.68 atm) of N_2 gas by submerging the fiber bundle in the DI water. For quality control of bundle fabrication, the gas flow of tested bundles (Alicat, USA) was verified; gas flow was 318 ± 59 cm^3 min^{-1} obtained at the open end of the hollow-fibers with 10 psig of applied N_2 gas. 100% CO_2 gas was delivered through the hollow-fiber membranes at various gas-supply pressures. Following a previous study,[23] the CO_2 flux (mg-C min^{-1}) was obtained using an 8-fiber membrane bundle at desired pressure supply from 2 to 10 psig with 100% CO_2 (Matheson, Phoenix) and conducted in an independently duplicate setting. The net inorganic-carbon increase within a 1 h time window was quantified by the Total Organic Carbon analyzer (Teledyne Tekmar Lotix, USA), and the transfer rates of 0.15−0.39 mg-C min^{-1} corresponded to 2−10 psig, respectively.

2.3. Light Utilization Efficiency of POF-NH_2-MIL-101(Fe). Photon irradiance was measured at multiple locations for the optical fiber, including total light input, the refraction of light side-emission, and light transmission (Figure S8). Light was delivered into the POF using a monochromatic LED light (3.0 W, λ = 440 nm, Uxcell, China) with an applied voltage of 5.4 V and a current of 0.55 A. Light-energy intensity (μW cm^{-2}) was measured every 2 cm apart by a spectrophotoradiometer (Avantes AvaSpec-2048 L, Louisville, CO, USA) equipped with a 600 μm jacketed silica fiber optic cable (FC-UV600−1-ME-SR) and a cosine corrector (CosC) attached to collect light using a radiometer (CC-UV/vis/NIR-8MM). Details of the light measurements are provided in Text S5. All measurements were performed using triplicate fibers.

Intensity denotes the directional energy density of a light ray (μW cm^{-2}), calculated by multiplying the energy density by the velocity vector of the light. Power, on the other hand, refers to the radiant or intensity flux received on a surface or the cumulative energy of each photon collected on a surface. Therefore, eq 1 embodies a conservation of power based on intensity (μW cm^{-2}) and the areas irradiated:

$$P_{\text{Abs(bare PMMA POF)}} = P_0 - P_T - P_S - P_U \quad (1)$$

where P_0 and P_T are the power (μW) entering and exiting (at the 20-cm distal end) the POF (Figure S8A). P_0 and P_T are calculated from the measured irradiance entering (I_0) and exiting (I_T) the 20-cm long POF multiplied by the POF cross-sectional area (πr^2). P_S is the scattering power due to side emission on the outer POF surface, where the photocatalyst is located. P_S is calculated by integrating the area under the curve of side-emitted light scattering intensity ($I_{S,x}$) measured every 2 cm along the 20 cm fiber length (x from 0 to 20 cm) using Origin 2018 version b.9.5.0.193, and then accounting for the outer surface area ($2\pi r$) of the fiber where the catalyst is located; the POF diameter is 3 mm (r = 0.15 cm). The percentages of power and intensity for the entire POF length are provided by eq 2 through eq 4:

$$P_{\text{Abs(bare PMMA POF)}}(\%) = \frac{P_0 - P_T - P_S - P_U}{P_0} \times 100\% \quad (2)$$

$$I_S(\%) \approx \frac{P_S}{P_0} \times 100\% = \frac{2\pi r \int_{x=0\text{ cm}}^{x=20\text{ cm}} I_{S,x}\, dx}{P_0} \times 100\% \quad (3)$$

$$I_U(\%) \approx \frac{P_U}{P_0} \times 100\% = \frac{P_0 - P_{\text{Abs}} - P_S - P_T}{P_0} \times 100\% \quad (4)$$

Where some energy is lost due to absorbance within the PMMA material of the POF ($P_{\text{Abs(bare PMMA POF)}}$ (%)), while other energy is scattered or utilized by the catalyst. Catalysts are activated by the intensity of light, and irradiance signifies the radiant flux over a real surface (μW cm^{-2}). Therefore, we consider the percentage of irradiance, as conservation relies on the intensity of each wave, for the amount of side-emitted light (I_S(%)) or light utilized by the photocatalyst (I_U(%)), which are approximately equivalent to the ratios of P_S or P_U to P_0, respectively.

2.4. Integrated Dual-Fiber Reactor System for Photocatalytic HCOOH Generation. Photocatalytic HCOOH production was evaluated in a photocatalytic dual-fiber reactor (Figure 1) that combined the modified POF and HFMs in two parallel and connected glass columns (0.8 cm diameter; 18 cm reactor length), each having a 10 mL total volume. One 20-cm long bare or coated POF (i.e., 20.7 cm^2 of outer surface area) and a ∼15-cm long HFM bundle were mounted in separate glass columns and connected using Versilon A-60-N tubing (Masterflex, MFLX06404-25). Ultrapure water (18.2 MΩ cm, pH ∼ 7.1) in the column was purged with N_2 gas for 2 h to remove dissolved oxygen before placing the water into the

https://doi.org/10.1021/acs.est.3c10274
Environ. Sci. Technol. 2024, 58, 13717−13725

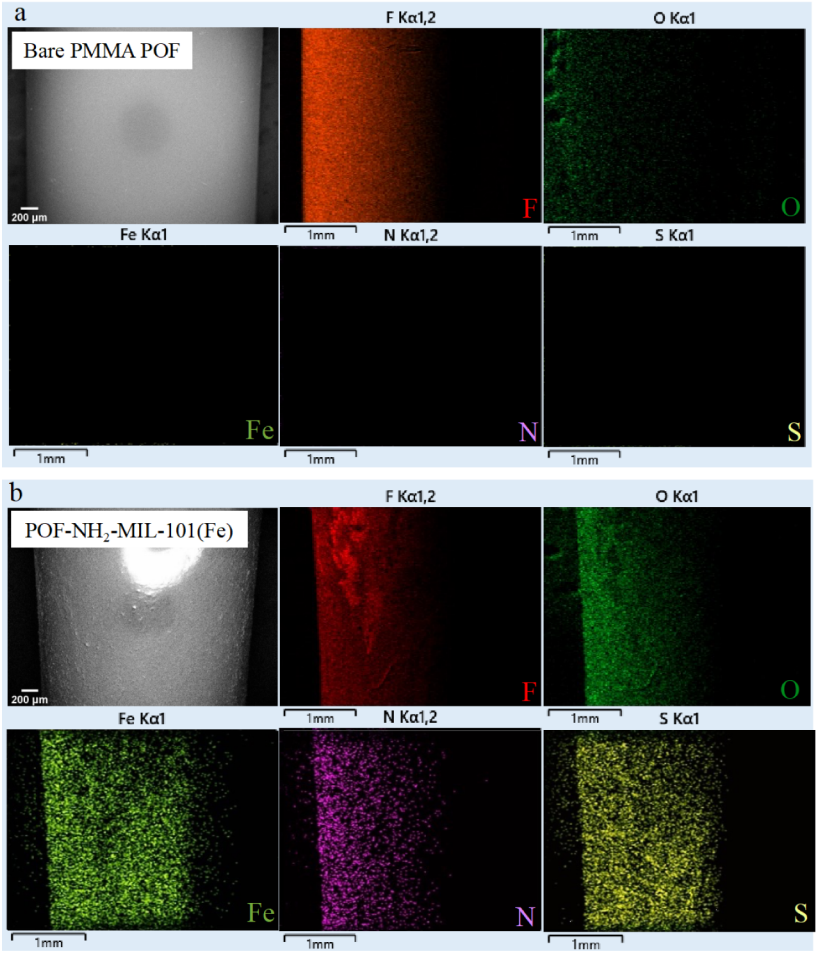

Figure 2. SEM images and EDS elemental mappings of (a) uncoated POF and (b) POF-NH_2-MIL-101(Fe) (34 μg cm^{-2}).

reactor. The reactor was continuously mixed by circulating water through the reactor system at a flow rate of 130 mL min^{-1} (Master Flex pump, model 7520-40, Cole-Parmer Instrument Company, USA). The experiment had a 2 h duration, and 1 mL liquid aliquots were collected from the reactor every 30 min (the reaction volume was reduced ~8% after all samplings) and analyzed for pH (i.e., maintained at ~3.8) and $HCOOH_{(aq)}$. pH was measured using a calibrated Lab 860 pH meter (Schott, Germany). Gas samples were collected from the headspace/gas bag with a 1 mL GC syringe and analyzed for $CO_{(g)}$ and $H_{2(g)}$. For selected experiments, potassium iodide (10 mM, KI) as an electron donor (electron−hole scavenger) was added to the initial deoxygenated water to give 3 mM KI as the final concentration; adding KI was used to gain an understanding of hole scavenging on photocatalytic CO_2 reduction.[24]

2.5. HCOOH, $CO_{(g)}$, $CO_{2(g)}$, and $H_{2(g)}$ Measurements. Formate was quantified by ion chromatography (IC). 1 mL samples were filtered using a 0.2-μm polyvinylidene fluoride filter prior to IC analysis (IC 930, Metrohm). The IC had a Metrosep A Supp 5-250/4.0 column and was run with an eluent of 1-mM sodium bicarbonate ($NaHCO_3$) plus 3.2 ppm sodium carbonate (Na_2CO_3) at a flow rate of 0.7 mL min^{-1}. Gaseous products ($CO_{(g)}$, $CO_{2(g)}$, and $H_{2(g)}$) were analyzed with a gas chromatograph (GC) (Shimadzu GC 2010) equipped with a thermal conductivity detector (TCD) held at 200 °C. The packed column (Carboxen 1010 PLOT, 30 m length) having a 0.53-μm inner diameter was operated isothermally at 230 °C and with ultrahigh purity argon (>99.999%) as the carrier gas at a flow rate of 40 mL min^{-1}. The gas volume in the Teflon bag was measured by a 60 mL gastight syringe. The concentrations of gas samples were utilized to calculate each value in grams using the ideal gas equation.

2.6. Performance Metrics. The quantum efficiency (Φ_{QE}) for photocatalytic HCOOH generation was calculated from

$$\Phi_{QE}(\%) = \frac{C_{HCOOH}}{\text{mol}_{photons}} \times 100\% \quad (5)$$

where C_{HCOOH} is the number of moles of HCOOH generated and $\text{mol}_{photons}$ is the moles of photons launched into the fiber; details on the computation are provided in Text S4.

The selectivity of CO_2 reduction to produce different carbon-based products considered two products (HCOOH and CO) based upon the following reduction half-reactions 6and 7 vs normal hydrogen electrode (NHE):[25]

$$CO_2 + 2H^+ + 2e^- \rightarrow HCOOH \quad E^0 = -0.61 \text{ V vs NHE} \quad (6)$$

$$CO_2 + 2H^+ + 2e^- \rightarrow CO \quad E^0 = -0.53 \text{ V vs NHE} \quad (7)$$

The total carbon delivered to the system was calculated using

https://doi.org/10.1021/acs.est.3c10274
Environ. Sci. Technol. 2024, 58, 13717−13725

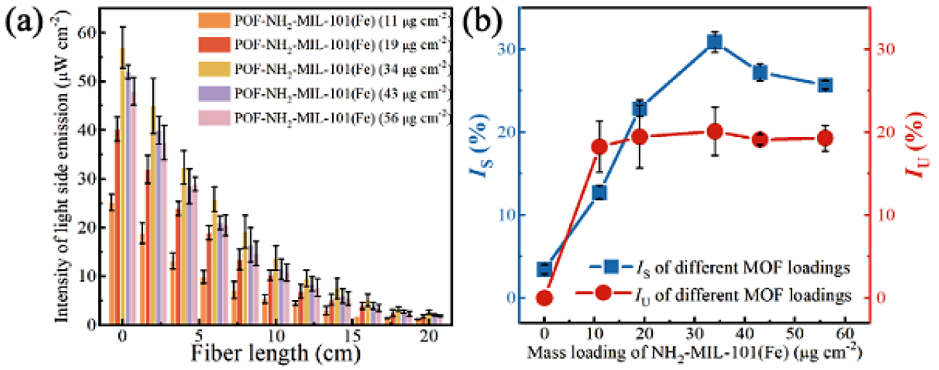

Figure 3. (a) Side-emitted light intensity along a 20 cm POF for different mass loadings by multiple coatings using 5 g of NH_2-MIL-101(Fe) L^{-1} and (b) light side-emission and -harvesting efficiencies of pristine and modified POFs. The I_S(%) and I_U(%) values changed with mass loadings of NH_2-MIL101(Fe) (μg cm^{-2}) exposed to 440 nm LED light (3 W) irradiation. The computation of side-emitted light for 0−10 g NH_2-MIL-101(Fe) L^{-1} slurries is summarized in Figures S9 and S10 and Table S2.

$$\text{Total carbon (TC, g)} = (\text{CO}_2 \text{ flux (C, g h}^{-1}) \times \text{duration (h)} \quad (8)$$

where CO_2 flux (C·g h^{-1}) was obtained using an 8-fiber membrane bundle at the specified pressure, as described in Section 2.2. Additionally, the gaseous samples were quantified for their concentrations with GC, as described in Section 2.5. No other carbon-containing compounds were identified by HPLC (Shimadzu, Japan) equipped with an Aminex HPX-87H column. All species for the carbon mass balance were converted to the unit of grams C. The mass of aqueous CO_2 at the end of the 2-h experiments was computed by the difference (all terms are in g C): $C-CO_{2\,(aq)}$ = Total C delivered (from the 2-h CO_2 delivery capacity)[23] − C-formate (from IC concentration multiplied by the liquid volume) − $C-CO_{2(g)}/CO_{(g)}$ (from the headspace CO_2 concentration by GC multiplied by the gas volume).

The conversion efficiency (%) for photocatalytic CO_2 reduction was also quantified for HCOOH and CO using the following relationships:

$$\text{HCOOH conversion (\%)} = \frac{\text{produced HCOOH}_{(aq)}\text{(g C)}}{\text{produced Total carbon(g C)}} \times 100\% \quad (9)$$

$$\text{CO conversion (\%)} = \frac{\text{produced CO}_{(g)}\text{(g C)}}{\text{produced Total carbon (g C)}} \times 100\% \quad (10)$$

The energy consumption of photocatalytic CO_2-to-HCOOH (kWh mol_{HCOOH}^{-1}) was computed from

$$\text{Energy consumption (kWh mol}^{-1}) = \frac{\text{kW} \times t}{m} \quad (11)$$

where kW is the light energy utilized by the photocatalytic layers, t is the time (hour), and m is the mole of HCOOH.

3. RESULTS AND DISCUSSION

3.1. Characterization of POF-NH_2-MIL-101(Fe). The characteristics of amine-functionalized Fe-based MOF, encompassing crystalline structure, functional groups, element states, band gap, and SEM analysis, are illustrated in Figures S1−S7. The morphologies and particle sizes of pristine NH_2-MIL-101(Fe) and POF-NH_2-MIL-101(Fe) were characterized by SEM and EDS. Figures 2 and S1 show electron-microscope images with elemental distributions for the exterior surface of uncoated POF and POF-MIL-101(Fe). The surface of bare POF contained only O, F, and C, since the two elements form the basic composition of the PMMA polymer with a fluorinated cladding layer (Figure 2a). The POF coated with NH_2-MIL-101(Fe) indicated a uniform surface coverage of Fe and N (Figure 2b). Results of Fe quantification by ICP-MS are described in more detail below but ranged from 0 on the bare fiber to 34 μg cm^{-2} for the MOF-coated POF (i.e., POF-NH_2-MIL-101(Fe)). Characterization of multiple fibers provided reproducible results. Overall, the dip-coating process successfully produced POF-NH_2-MIL-101(Fe) that could be used in the dual-fiber reactor system (Figure 1).

3.2. Optimizing Light Utilization through NH_2-MIL-101(Fe) Coating. Photocatalytic activity capable of converting aqueous inorganic carbon to organic carbon is driven by the delivery of visible light to the surface of the POF on which NH_2-MIL-101(Fe) is embedded. The bare fiber side emits light because of refractive index differences between the PMMA cladding. When the MOF is applied to the fiber surface, it enables the absorption and utilization of light by NH_2-MIL-101(Fe), as illustrated in eqs 1 and 2. Figure 3a shows intensities of side-emitted 440 nm light along a 20 cm length of POF with different NH_2-MIL-101(Fe) loadings. Bare POFs exhibited a side emission of 11 μW cm^{-2} at the proximal end, and it exponentially declined along the 20 cm length to 1 μW cm^{-2} at the distal end. For a POF loaded with 10 μg cm^{-2} NH_2-MIL-101(Fe), the side-emission light intensity increased to 21 μW cm^{-2} at the proximal end and 1 μW cm^{-2} at the distal end. A higher NH_2-MIL-101 loading (i.e., 34 μg cm^{-2}) led to increased side-emitted light, with values reaching 57 μW cm^{-2} at the proximal end and 3 μW cm^{-2} at the distal end. The observed enhancements in side emission can be attributed to alterations in the refractive index and/or the introduction of additional Rayleigh scattering at the POF−water interface resulting from the NH_2-MIL-101(Fe) coating.[26]

The highest I_S(%) and optimal light utilization (I_U(%)), calculated by eq 4 and depicted in Figure 3b, indicate that a mass loading of 34 μg cm^{-2} NH_2-MIL-101(Fe) yielded 31% I_S and 21% I_U. Notably, the trends in I_S(%) and I_U(%) consistently showed that excessive photocatalyst loading compromised both metrics. The alignment of I_S(%) and I_U(%) results underscores that an optimal mass loading

https://doi.org/10.1021/acs.est.3c10274
Environ. Sci. Technol. 2024, 58, 13717−13725

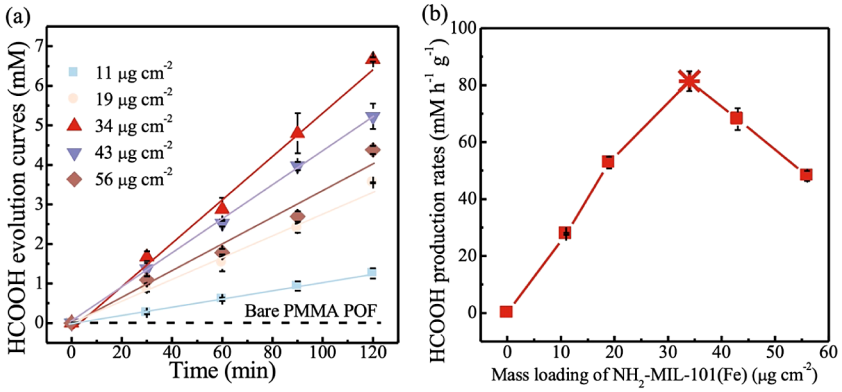

Figure 4. (a) Photocatalytic CO_2 reduction followed zero-order kinetics for HCOOH evolution with various NH_2-MIL-101(Fe) on POF loadings and (b) the normalized HCOOH production rates peaked at the surface loading of 34 μg cm^{-2} NH_2-MIL-101(Fe). Irradiation was 3 W with a 440 nm LED light.

maximized side emissions, thus contributing to increased photon utilization. The highest values for I_S(%) and I_U(%) were attained with the 3-cycle coating, resulting from the deposition of 34 μg cm^{-2} NH_2-MIL-101(Fe). Therefore, we denote 34 μg cm^{-2} of NH_2-MIL-101(Fe) as the "optimized loading for light utilization".

3.3. HCOOH Production. The dual-fiber reactor successfully generated high yields of HCOOH. Figure 4 demonstrates that the photocatalytic generation of HCOOH, CO, and H_2 occurred only for MOF-coated POFs; no other carbon products were identified. Figure 4a illustrates the rapid formation of formic acid with rates varying according to MOF loadings. The kinetics of formic acid production were well represented by pseudozero order kinetics, and Table S3 summarizes values of the best-fit zero-order rate constant (k). The normalized k values in Figure 4b reveal maximum photocatalytic activity for the 34 μg cm^{-2} mass loading of POF-NH_2-MIL-101(Fe), which is consistent with the highest values for I_S(%) and I_U(%) shown in Figure 3. The maximum formic-acid-production rate reached 82 mM h^{-1} g^{-1}, approximately twice as high as rates observed for the mass loading of 56 μg cm^{-2} NH_2-MIL-101(Fe). Thus, the same mass loading (34 μg cm^{-2}) that was optimized for light utilization also resulted in the maximum rate of formic-acid production.

The maximum photocatalytic activity of the POF-NH_2-MIL-101(Fe) was 18-fold higher than the rate (~5 mM h^{-1}g^{-1}) for a slurry containing NH_2-MIL-101(Fe) catalyst (i.e., the same catalyst weight coated on the optical fiber) under identical reactor configuration and irradiation conditions (Figures 5 and S11). The slurry approach, wherein complete mixing occurred, resulted in the continuous movement of photocatalysts in and out of zones where the photons were delivered into the water. The optimized activity of POF-NH_2-MIL-101(Fe) was about 1.8-fold higher than the rate obtained from loading of 39 μg cm^{-2} without R-NH_2 decorating (i.e., MIL-101(Fe)), indicating that the pivotal role of the amine groups improved $CO_{2(aq)}$ capture, thereby enhancing the adsorption of the carbonyl group (C═O) and facilitating the photocatalytic reduction. In contrast, MIL-101(Fe) catalysts lacking $-NH_2$ modification showed inferior performance.

The net effect of the enhanced and consistent irradiation of the MOF on the POF led to the dual-fiber system achieving a remarkably high quantum efficiency (QE). The QE was 12% for the POF with optimal loading conditions, which surpassed

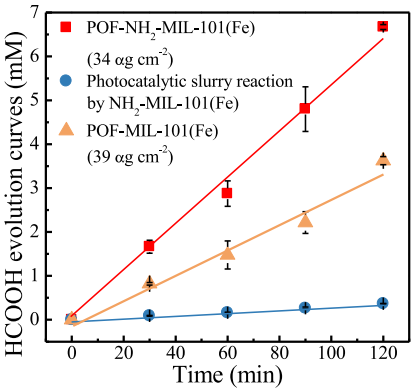

Figure 5. HCOOH generation of POF-NH_2-MIL-101(Fe), POF-MIL-101(Fe), and a photocatalytic NH_2-MIL-101(Fe) slurry reaction. Irradiation was from a 3-W LED at 440 nm.

the QE obtained from photocatalytic slurry from other photocatalysts (e.g., Au/TiO_2, ZnS, or Cu_2O) by 1.2- to 60-fold (Table S4).[8,27−30] Notably, energy consumption with the optimal condition was only 0.6 kWh mol$^{-1}_{HCOOH}$, which was about several magnitudes lower than photocatalytic CO_2 reduction in a slurry for other catalysts (Table S4).[8,27−30] Higher energy-conversion efficiencies were achieved through the dual efficiencies of CO_2 delivery via the gas-permeable membrane, which prevented the loss of CO_2 from water, and through the high quantum yield achieved using the POF platform.

The POF with the optimal MOF loading had good reusability for CO_2 reduction. As illustrated in Figure S12, consistent formate generation occurred over five sequential tests, each having a 2-h duration. The calculated k values for HCOOH production were similar for each cycle ($p \geq 0.05$). While additional testing will be required to assess the long-term stability of the MOF over months or years of operation, the results in Figure S12 document the reusability of NH_2-MIL-101(Fe).

Formate was the dominant product, although other reduced gases (i.e., CO and H_2) were generated during photocatalytic CO_2 reduction. For the optimal mass loading (34 μg cm^{-2}), the production curves of CO and H_2 (Figure 6a) were linear, reaching maximum concentrations of 1.4 × 10^{-2} and 2.5 × 10^{-2} mmol, respectively. As the conductive-to-valence band gap of NH_2-MIL-101(Fe) was not compatible with the water

https://doi.org/10.1021/acs.est.3c10274
Environ. Sci. Technol. 2024, 58, 13717−13725

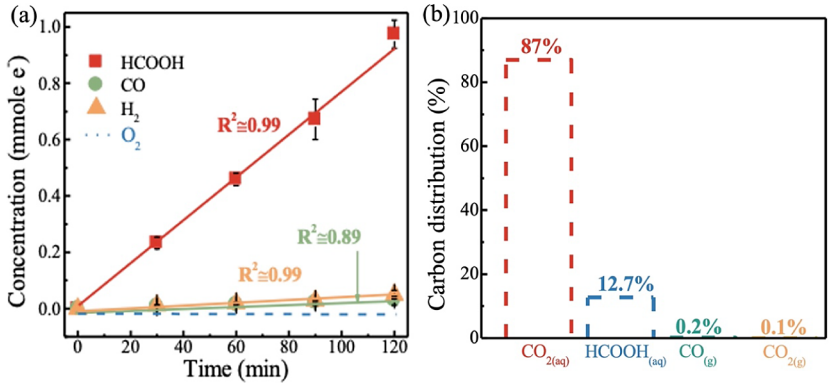

Figure 6. (a) Generation curves for HCOOH, CO, H_2, and O_2 for POF-NH_2-MIL-101(Fe) (34 μg cm^{-2}) and (b) carbon mass balance on products of the dual fiber system using the optimal POF-NH_2-MIL-101(Fe) (34 μg cm^{-2}) with a 440-nm LED (3W) and a CO_2 flux at 0.39 mg-C min^{-1} from the HFM.

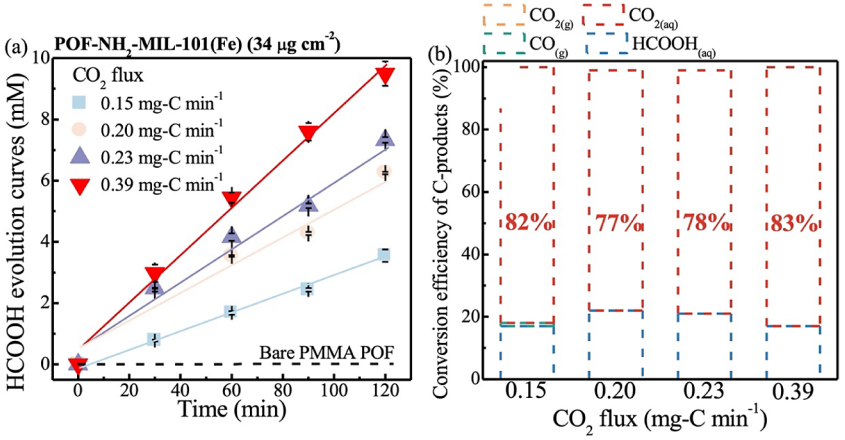

Figure 7. Carbon conversion for photocatalytic CO_2 reduction using 34 μg cm^{-2} NH_2-MIL-101(Fe) for different $CO_{2(g)}$-supply pressures, 3 mM KI, and irradiation at 3 W with a 440 nm LED: (a) CO_2-fluxes and (b) carbon mass balance at the end of 2 h.

oxidation potential,[31] O_2 evolution did not occur during the photocatalysis. On an electron basis (mmol electrons per eqs 6 and 7), the optimal fiber system was 34- and 19-fold more selective toward HCOOH than toward CO and H_2, respectively. Figure 6b, which presents the carbon mass balance, shows that 12.7% of the CO_2 transferred from the membranes was routed to HCOOH, with CO only 0.2%; $CO_{2(aq)}$ and $CO_{2(g)}$ accounted for 87.0 and 0.1% of the total input carbon, respectively. Thus, the CO_2-supply rate (0.39 mg-C min^{-1}) exceeded the photocatalytic CO_2-reduction capacity.

In order to enhance the conversion of CO_2 to HCOOH, we varied the CO_2-supply pressure within the range of 2−10 psig, which gave delivery capacities ranging from 0.15 to 0.39 mg-C min^{-1}. Also, we performed experiments in the presence of potassium iodide (KI), an electron−hole scavenger that should reduce the oxidation of formic acids by electron holes. The introduction of potassium iodide (KI) enhanced the HCOOH-production rate, increasing it from 82 to 116 mM h^{-1} g^{-1} (Figure 4a vs Figure 6a).

Figure 7a show that the highest HCOOH-production rate (116 mM h^{-1} g^{-1}; $k = 3.5 \times 10^{-4}$ mM s^{-1}) was achieved with the 10 psig CO_2 gas pressure. Notably, this rate is >2.7-fold higher than the value operated at 2 psig ($k = 1.9 \times 10^{-4}$ mM s^{-1}). $CO_{2(aq)}$ concentration was a key factor for the formate-production rate, and no formate was generated without a CO_2 supply (Figure S13). Carbon transfer efficiency (CTE) affects how much $CO_{2(g)}$ must be supplied to attain a given aqueous $CO_{2(aq)}$ concentration. In general, commercial spargers can achieve 20−40% CTE, while hollow-fiber membranes can approach 100% CTE for medium pH near or above neutral.[32,33] Bubbles formed by spargers can have the added disadvantage of disrupting the catalytic reaction by dispersing the light.

Figure 7b reveals that the highest carbon-conversion efficiency (23%) of CO_2 to HCOOH was obtained with 3 psig of CO_2 (0.2 mg-C min^{-1}), and the efficiency dropped to 17% at 10 psig (0.39 mg-C min^{-1}) (Table S5). As the water did not have a buffer to maintain the pH, a low pH of 3.8−4.0 developed during CO_2(g) delivery. The low pH led to CO_2 off-gassing, which lowered the carbon-transfer efficiency.

4. ENVIRONMENTAL SIGNIFICANCE

Through coupling a POF coated with NH_2-MIL-101(Fe) for catalyzed CO_2 reduction and hollow-fiber membranes for efficient CO_2 delivery, the dual-fiber system gave a high-rate CO_2-to-HCOOH production, reaching as high as 116 mM h^{-1} g^{-1}. This rate is 25-fold greater than any corresponding value observed in a photocatalytic slurry system. The optimized condition achieved a 12% QE, which was about 18-fold higher than the QE obtained from photocatalytic NH_2-MIL-101(Fe) in a slurry reactor. The optimal NH_2-MIL-101(Fe) mass loading on the POF for formic acid production corresponded

https://doi.org/10.1021/acs.est.3c10274
Environ. Sci. Technol. 2024, 58, 13717−13725

to the loading that achieved the highest $I_S(\%)$ and $I_U(\%)$. This correspondence reinforces that a primary benefit of the optical fiber is superior light delivery to the photocatalysts because coating MOF photocatalysts on the POF surface enabled continuous exposure to light without relying on light penetration through the water column or reactor wall, as in slurry systems. In addition, the $I_S(\%)$ and $I_U(\%)$ from and with the POFs were correlated with CO_2 conversion, because an optical fiber with high side-emission allows more photons to be emitted across the cladding along the length of fibers, which led to higher quantum efficiency for CO_2 reduction. The hollow-fiber membranes provided effective bubble-free CO_2 delivery that enabled simple and robust control of the CO_2 mass transport that could be synchronized with the CO_2 flux needed to reduce CO_2 to HCOOH; the selectivity to HCOOH was up to 99%.

Scaling up the dual-fiber reactor can be optimized by increasing the specific surface areas of the MOF-coated POF and hollow-fiber membranes. The former can increase the volumetric production rate,[34] while the latter can match the CO_2-delivery rate to the CO_2-reduction rate while also maintaining high selectivity for HCOOH. Another strategy for improving performance would provide a pH buffer that does not allow the pH to decline, which allows CO_2 off-gassing. Finally, real-world application will not be with ultrapure water, prompting the need to examine limitations (e.g., fouling) and opportunities (e.g., pH buffering) associated with different water qualities.

■ ASSOCIATED CONTENT

Supporting Information

The Supporting Information is available free of charge at https://pubs.acs.org/doi/10.1021/acs.est.3c10274.

Synthesis of NH_2-decorated Fe-based MOF (NH_2-MIL-101(Fe)); solid-state characterization; quantum efficiency calculation; fabrication of hollow-fiber-membrane bundles; different loading of NH_2-MIL-101(Fe) on the optical fiber; $I_S(\%)$ and $I_U(\%)$ performance for the modified POFs with different mass loadings of NH_2-MIL-101(Fe); the zero-order kinetics of photocatalytic HCOOH production with different operating conditions; comparison of photocatalytic HCOOH generation with other nanophotocatalysts; conversion performance (%) and selectivity effects of C-products in a photocatalytic CO_2 reduction; photocatalyst characterization (i.e., XRD, FTIR, XPS, UV−visible, UPS, and SEM); light-measurements and estimated values utilized in energy balances; side-emitted light intensity along a 20 cm POF for different mass loadings; I_S and I_U performance (%) of pristine POF and modified POFs; HCOOH-generation curves of POF-NH_2-MIL-101(Fe) with 1−10 g NH_2-MIL-101(Fe) L^{-1} slurry for dip coatings; HCOOH generation for POF-NH_2-MIL-101(Fe) (34 $\mu g\ cm^{-2}$) with and without CO_2 conditions (PDF)

■ AUTHOR INFORMATION

Corresponding Authors

YenJung Sean Lai − *Biodesign Swette Center for Environmental Biotechnology, Arizona State University, Tempe, Arizona 85281, United States;* orcid.org/0000-0001-7611-8441; Email: Yen-Jung·Lai@asu.edu

Paul Westerhoff − *Engineering Research Center for Nanotechnology-Enabled Water Treatment (NEWT), School of Sustainable Engineering and the Built Environment, Arizona State University, Tempe, Arizona 85281, United States;* orcid.org/0000-0002-9241-8759; Email: P.WESTERHOFF@asu.edu

Authors

Tzu-Heng Wang − *Department of Biomedical Engineering and Environmental Sciences, National Tsing Hua University, Hsinchu 30013, Taiwan; Biodesign Swette Center for Environmental Biotechnology, Arizona State University, Tempe, Arizona 85281, United States; Engineering Research Center for Nanotechnology-Enabled Water Treatment (NEWT), School of Sustainable Engineering and the Built Environment, Arizona State University, Tempe, Arizona 85281, United States*

Cheng-Kuo Tsai − *Emergency Response Information Center, National Yunlin University of Science and Technology, Yunlin 64002, Taiwan*

Han Fu − *Engineering Research Center for Nanotechnology-Enabled Water Treatment (NEWT), School of Sustainable Engineering and the Built Environment, Arizona State University, Tempe, Arizona 85281, United States*

Ruey-An Doong − *Institute of Analytical and Environmental Sciences, National Tsing Hua University, Hsinchu 30013, Taiwan;* orcid.org/0000-0002-4913-0602

Bruce E. Rittmann − *Biodesign Swette Center for Environmental Biotechnology, Arizona State University, Tempe, Arizona 85281, United States; Engineering Research Center for Nanotechnology-Enabled Water Treatment (NEWT), School of Sustainable Engineering and the Built Environment, Arizona State University, Tempe, Arizona 85281, United States;* orcid.org/0000-0002-3678-149X

Complete contact information is available at: https://pubs.acs.org/10.1021/acs.est.3c10274

Notes

The authors declare the following competing financial interest(s): The authors have submitted a patent disclosure on the dual-fiber technology for photocatalytic systems.

■ ACKNOWLEDGMENTS

This work was partially funded by the Ministry of Science and Technology (MOST, No. 109-2926-I-007-505; Taiwan), the LightWorks program, and the Biodesign Swette Center for Environmental Biotechnology at Arizona State University, as well as the National Science Foundation Nanosystems Engineering Research Center for Nanotechnology-Enabled Water Treatment (EEC-1449500), and NASA (80NSSC19C0564). We would like to acknowledge the Eyring Materials Center at Arizona State University, supported in part by the National Science Foundation (ECCS-2025490), as well as the generous support of Founder & Chief Technology Officer Mr. Randy Dahl from Industrial Fiber Optics (Tempe, AZ, USA).

■ REFERENCES

(1) Eskander, S. M. S. U.; Fankhauser, S. Reduction in Greenhouse Gas Emissions from National Climate Legislation. *Nat. Clim. Change* **2020**, *10* (8), 750−756.

(2) Waxman, A. R.; Khomaini, A.; Leibowicz, B. D.; Olmstead, S. M. Emissions in the Stream: Estimating the Greenhouse Gas Impacts of an Oil and Gas Boom. *Environ. Res. Lett.* **2020**, *15* (1), 014004.
(3) Liu, Y.; Sun, J.; Huang, H.; Bai, L.; Zhao, X.; Qu, B.; Xiong, L.; Bai, F.; Tang, J.; Jing, L. Improving CO_2 Photoconversion with Ionic Liquid and Co Single Atoms. *Nat. Commun.* **2023**, *14* (1), 1457.
(4) Akhter, P.; Farkhondehfal, M. A.; Hernández, S.; Hussain, M.; Fina, A.; Saracco, G.; Khan, A. U.; Russo, N. Environmental Issues Regarding CO_2 and Recent Strategies for Alternative Fuels through Photocatalytic Reduction with Titania-Based Materials. *J. Environ. Chem. Eng.* **2016**, *4* (4), 3934−3953.
(5) Roy, S. C.; Varghese, O. K.; Paulose, M.; Grimes, C. A. Toward Solar Fuels: Photocatalytic Conversion of Carbon Dioxide to Hydrocarbons. *ACS Nano* **2010**, *4* (3), 1259−1278.
(6) Weilhard, A.; Argent, S. P.; Sans, V. Efficient Carbon Dioxide Hydrogenation to Formic Acid with Buffering Ionic Liquids. *Nat. Commun.* **2021**, *12* (1), 231.
(7) Shit, S. C.; Shown, I.; Paul, R.; Chen, K.-H.; Mondal, J.; Chen, L.-C. Integrated Nano-Architectured Photocatalysts for Photochemical CO_2 Reduction. *Nanoscale* **2020**, *12* (46), 23301−23332.
(8) Baran, T.; Wojtyła, S.; Dibenedetto, A.; Aresta, M.; Macyk, W. Zinc Sulfide Functionalized with Ruthenium Nanoparticles for Photocatalytic Reduction of CO_2. *Appl. Catal., B* **2015**, *178*, 170−176.
(9) Taki, T.; Strassburg, M. Review—Visible LEDs: More than Efficient Light. *ECS J. Solid State Sci. Technol.* **2020**, *9* (1), 15017.
(10) Raptopoulou, C. P. Metal-Organic Frameworks: Synthetic Methods and Potential Applications. *Materials* **2021**, *14* (2), 310.
(11) Peng, C.; Reid, G.; Wang, H.; Hu, P. Perspective: Photocatalytic Reduction of CO_2 to Solar Fuels over Semiconductors. *J. Chem. Phys.* **2017**, *147* (3), 030901.
(12) Low, J.; Yu, J.; Jaroniec, M.; Wageh, S.; Al-Ghamdi, A. A. Heterojunction Photocatalysts. *Adv. Mater.* **2017**, *29* (20), 1601694.
(13) Wang, M.; Dong, X.; Meng, Z.; Hu, Z.; Lin, Y.-G.; Peng, C.; Wang, H.; Pao, C.-W.; Ding, S.; Li, Y.; Shao, Q.; Huang, X. An Efficient Interfacial Synthesis of Two-Dimensional Metal−Organic Framework Nanosheets for Electrochemical Hydrogen Peroxide Production. *Angew. Chem., Int. Ed.* **2021**, *60* (20), 11190−11195.
(14) Zhang, Z.; Li, X.; Liu, B.; Zhao, Q.; Chen, G. Hexagonal Microspindle of NH_2 -MIL-101(Fe) Metal−Organic Frameworks with Visible-Light-Induced Photocatalytic Activity for the Degradation of Toluene. *RSC Adv.* **2016**, *6* (6), 4289−4295.
(15) Sezemsky, P.; Burnat, D.; Kratochvil, J.; Wulff, H.; Kruth, A.; Lechowicz, K.; Janik, M.; Bogdanowicz, R.; Cada, M.; Hubicka, Z.; Niedziałkowski, P.; Białobrzeska, W.; Stranak, V.; Śmietana, M. Tailoring Properties of Indium Tin Oxide Thin Films for Their Work in Both Electrochemical and Optical Label-Free Sensing Systems. *Sens. Actuators, B* **2021**, *343*, 130173.
(16) Helal, A.; Shaheen Shah, S.; Usman, M.; Khan, M. Y.; Aziz, M. A.; Mizanur Rahman, M. Potential Applications of Nickel-Based Metal-Organic Frameworks and Their Derivatives. *Chem. Rec.* **2022**, *22* (7), No. e202200055.
(17) Lee, H. M.; Youn, I. S.; Saleh, M.; Lee, J. W.; Kim, K. S. Interactions of CO_2 with Various Functional Molecules. *Phys. Chem. Chem. Phys.* **2015**, *17* (16), 10925−10933.
(18) Wang, T.-H.; Chen, M.-J.; Lai, Y. S.; Doong, R.; Westerhoff, P.; Rittmann, B. High-Efficiency Photocatalytic H_2O_2 Production in a Dual Optical− and Membrane−Fiber System. *ACS Sustainable Chem. Eng.* **2023**, *11* (16), 6465−6473.
(19) Zhong, H.; Fujii, K.; Nakano, Y.; Jin, F. Effect of CO_2 Bubbling into Aqueous Solutions Used for Electrochemical Reduction of CO_2 for Energy Conversion and Storage. *J. Phys. Chem. C* **2015**, *119* (1), 55−61.
(20) Kanth, N.; Xu, W.; Prasad, U.; Ravichandran, D.; Kannan, A. M.; Song, K. PMMA-TiO_2 Fibers for the Photocatalytic Degradation of Water Pollutants. *Nanomaterials* **2020**, *10* (7), 1279.
(21) Li, X.; Guo, W.; Liu, Z.; Wang, R.; Liu, H. Quinone-Modified NH_2-MIL-101(Fe) Composite as a Redox Mediator for Improved Degradation of Bisphenol A. *J. Hazard. Mater.* **2017**, *324*, 665−672.
(22) Huang, P.; Yao, L.; Chang, Q.; Sha, Y.; Jiang, G.; Zhang, S.; Li, Z. Room-Temperature Preparation of Highly Efficient NH2-MIL-101(Fe) Catalyst: The Important Role of − NH_2 in Accelerating Fe(III)/Fe(II) Cycling. *Chemosphere* **2022**, *291*, 133026.
(23) Shesh, T.; Eustance, E.; Lai, Y.-J.; Rittmann, B. E. Characterization of CO_2 Flux through Hollow-Fiber Membranes Using PH Modeling. *J. Membr. Sci.* **2019**, *592*, 117389.
(24) Winkler, R. Iodine—A Potential Antioxidant and the Role of Iodine/Iodide in Health and Disease. *Nat. Sci.* **2015**, *07* (12), 548−557.
(25) Fu, J.; Jiang, K.; Qiu, X.; Yu, J.; Liu, M. Product Selectivity of Photocatalytic CO_2 Reduction Reactions. *Mater. Today* **2020**, *32*, 222−243.
(26) Song, Y.; Ling, L.; Westerhoff, P.; Shang, C. Evanescent Waves Modulate Energy Efficiency of Photocatalysis within TiO_2 Coated Optical Fibers Illuminated Using LEDs. *Nat. Commun.* **2021**, *12* (1), 4101.
(27) Pan, H.; Steiniger, A.; Heagy, M. D.; Chowdhury, S. Efficient Production of Formic Acid by Simultaneous Photoreduction of Bicarbonate and Oxidation of Glycerol on Gold-TiO_2 Composite under Solar Light. *J. CO2 Util.* **2017**, *22*, 117−123.
(28) Pan, H.; Heagy, M. D. Plasmon-Enhanced Photocatalysis: Ag/TiO2 Nanocomposite for the Photochemical Reduction of Bicarbonate to Formic Acid. *MRS Adv.* **2019**, *4* (7), 425−433.
(29) Pan, H.; Chowdhury, S.; Premachandra, D.; Olguin, S.; Heagy, M. D. Semiconductor Photocatalysis of Bicarbonate to Solar Fuels: Formate Production from Copper(I) Oxide. *ACS Sustainable Chem. Eng.* **2018**, *6* (2), 1872−1880.
(30) Tian, Y.; Zhou, Y.; Zong, Y.; Li, J.; Yang, N.; Zhang, M.; Guo, Z.; Song, H. Construction of Functionally Compartmental Inorganic Photocatalyst−Enzyme System via Imitating Chloroplast for Efficient Photoreduction of CO_2 to Formic Acid. *ACS Appl. Mater. Interfaces* **2020**, *12* (31), 34795−34805.
(31) Navarro Yerga, R. M.; Alvarez-Galván, M. C.; Vaquero, F.; Arenales, J.; Fierro, J. L. G. Chapter 3 - Hydrogen Production from Water Splitting Using Photo-Semiconductor Catalysts. In *Renewable Hydrogen Technologies: Production, Purification, Storage, Applications and Safety* Gandía, L. M.; Arzamendi, G.; Diéguez, P. M., Eds.; Elsevier: Amsterdam, 2013; pp. 4361. DOI: .
(32) Lai, Y. S.; Eustance, E.; Shesh, T.; Rittmann, B. E. Enhanced Carbon-Transfer and -Utilization Efficiencies Achieved Using Membrane Carbonation with Gas Sources Having a Range of CO_2 Concentrations. *Algal Res.* **2020**, *52*, 102098.
(33) Acién Fernández, F. G.; González-López, C. V.; Fernández Sevilla, J. M.; Molina Grima, E. Conversion of CO_2 into biomass by microalgae: how realistic a contribution may it be to significant CO_2 removal. *Appl. Microbiol. Biotechnol.* **2012**, *96* (3), 577−586.
(34) Wang, T.-H.; Zhao, Z.; Garcia-Segura, S.; Ling, L.; Doong, R.; Westerhoff, P. Flexible Fiber Optoelectrodes Integrating Perovskite-Nafion-ITO Layers for Efficient Photoelectrocatalytic Water Purification. *Appl. Catal., B* **2024**, *342*, 123397.

https://doi.org/10.1021/acs.est.3c10274
Environ. Sci. Technol. 2024, 58, 13717−13725